Chemical Science

ROYAL SOCIETY OF CHEMISTRY

EDGE ARTICLE

View Article Online
View Journal

Cite this: DOI: 10.1039/d6sc01229a

All publication charges for this article have been paid for by the Royal Society of Chemistry

Selective white phosphorus activation and functionalization with inorganic Grignard reagents

Franziska Gilch, [a] Jan Brossette, [b] Franz Westermair, [c] Wagner Menezes da Silva, [c] Gábor Balázs, [a] Ruth M. Gschwind, *[c] Hendrik Zipse *[b] and Robert Wolf *[a]

We describe the targeted and selective functionalization of white phosphorus (P_4) using 'inorganic Grignard reagents'. Reactions of the Fe–Mg complexes [(^{Dipp}BDI)Mg(THF)$_x$Fp] (Fp = CpFe(CO)$_2$, **1**: $x = 0$; **1-THF**: $x = 1$, ^{Dipp}BDI = 2,6-diisopropylphenyl-1,3-diketiminate)) and [(^{Dipp}BDI)MgFp*] (**2**, Fp* = Cp*Fe(CO)$_2$) afford the compounds [(^{Dipp}BDI)Mg(THF)$_x$Fp(μ-P_4)] (**3**: $x = 0$; **3-THF**: $x = 1$) and [(^{Dipp}BDI)MgFp*(μ-P_4)] (**4**) featuring P_4^{2-} ligands with a 'butterfly' structure bridging Fe and Mg. The coordination of the β-diketiminate magnesium cations [(DippBDI)Mg]$^+$ plays a key role in stabilizing these reactive 'P_4-butterfly' anions through non-covalent Mg–P bonds and dispersion forces. Thermolysis or photolysis of **3-THF** and **4** afforded rare tetraphosphacyclopentadienolate complexes **7** and **8**. Complex **4** exhibits unmitigated reactivity towards a wide range of main group element electrophiles (^{i}PrNC^{i}Pr, Ph_2BCl, Ph_3SnCl, $(Me_3Si)_3SiCl$ and Mes_2PCl), furnishing rare examples of stable, mixed-substituted tetraphosphanes **9–13** as well as an octaphosphane **14** featuring a Sn_2P_8 core.

Received 11th February 2026
Accepted 3rd April 2026

DOI: 10.1039/d6sc01229a

rsc.li/chemical-science

Introduction

White phosphorus (P_4) is the only molecular allotrope of phosphorus stable at room temperature and serves as a crucial feedstock for phosphorus-based chemicals.[1] Because of its important role in the phosphorus industry and its multifaceted and often poorly predictable reactivity, the chemistry of P_4 is a subject of significant current interest. Although many procedures for P_4 activation using main-group elements and transition metals have been reported, the targeted, selective functionalization of the resulting polyphosphorus frameworks lags behind simple P_4 activation.[2]

The bicyclo[1.1.0]tetraphosphabutane motive ('P_4-butterfly') resulting from the cleavage of one P–P bond of the P_4 tetrahedron represents the first step in P_4 activation.[3,4] The synthesis of 'P_4-butterfly' compounds has been achieved by reaction of P_4 with main-group radicals and transition-metal-based radicals,[3] as well as using carbenes and heavier carbene analogues.[4] Reactions of this type result in the generation of symmetrical P_4-butterfly species of types **A** or **B** (Fig. 1). Due to the strong, covalent phosphorus-element bonds, these species typically exhibit attenuated reactivity and limited potential for further functionalization. In contrast, the reaction of P_4 with charged nucleophiles affords highly reactive anions $[RP_4]^-$ (**C**), which tend to decompose quickly.[5,6] Nonetheless, alkali metal salts of type M[HP_4] have been characterised by ^{31}P NMR spectroscopy at low temperature.[5,7] Lammertsma and coworkers have reported that $[RP_4]^-$ anions (**C**) containing sterically demanding aryl groups or the Fp*$^-$ anion (Fp* = Cp*Fe(CO)$_2$, Cp* = C_5Me_5) can be stabilized by the coordination of boranes such as BPh_3 and $B(C_6F_5)_3$ to one of the wingtip phosphorus atoms (**D**, Fig. 1a, R = bulky aryl or Fp*).[8–12] However, the reactivity of these species has been limited to protonation and alkylation reactions, a [3 + 1] fragmentation reaction induced by PhNCO and Lewis acid coordination with BH_3, BPh_3, $W(CO)_5$ and [Au(IPr)]$^+$ [IPr = 1,3-bis(2,6-diisopropylphenyl)imidazolin-2-ylidene]. The P_4-butterfly species **E** resulting from the functionalization of **D** with R′X decomposes with R′ = H or Me, but can be isolated when sterically demanding alkyl groups such as Ph_3C are employed.[8,11,12]

Recently, we have shown that the combination of a redox-active 3d-metal cation with a main-group element, such as Ga, Si, Sn, or a redox non-innocent d-block element such as Zn, facilitates P_4 activation.[13] In contrast, the use of transition-metal-magnesium complexes ('inorganic Grignard reagents') for P_4 activation has hardly been explored,[14–16] despite recent studies demonstrating the significant potential of low-valent magnesium and calcium complexes for P_4 storage and activation (Fig. 1, complexes **F–H**, Fig. 1).[17,18] Here, we demonstrate that the inorganic Grignard reagents [(^{Dipp}BDI)Mg(THF)$_x$Fp] (**1**: $x = 0$; **1-THF**: $x = 1$, Fp = CpFe(CO)$_2$, ^{Dipp}BDI = 2,6-diisopropylphenyl-1,3-diketiminate) and [(^{Dipp}BDI)MgFp*] (**2**)

[a]Universität Regensburg, Institut für Anorganische Chemie, 93040 Regensburg, Germany. E-mail: robert.wolf@ur.de

[b]Ludwig-Maximilians-Universität München, Institut für Chemie, Butenandtstr. 5-13, 81377 München, Germany. E-mail: zipse@cup.uni-muenchen.de

[c]Universität Regensburg, Institut für Organische Chemie, 93040 Regensburg, Germany. E-mail: ruth.gschwind@ur.de

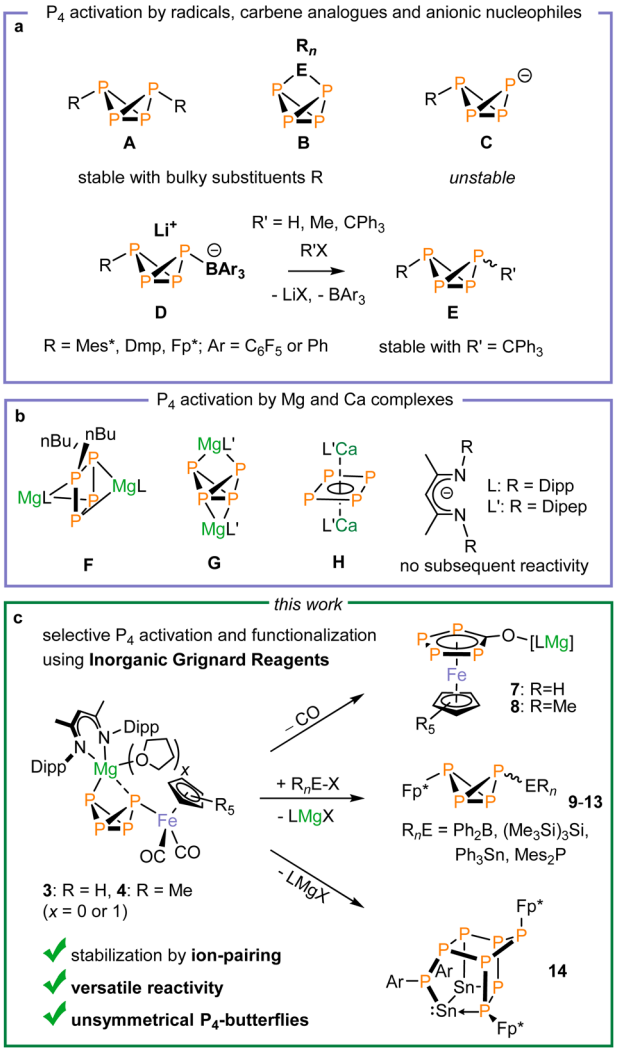

Fig. 1 (a) Bicyclo[1.1.0]tetraphosphabutanes and related anions **A**–**E** resulting from the reaction of P_4 with radicals, carbene analogues, and nucleophilic anions. (b) Reaction products of P_4 with BDI-stabilized Mg(II), Mg(I) and Ca(I) complexes. (c) Selective P_4 activation and functionalization enabled by Mg–Fe pairs (this work; Mes* = 2,4,6-$tBu_3C_6H_2$, Dmp = 2,6-Me_2-C_6H_3, Dipp = 2,6-diisopropylphenyl, Dipep = 2,6-diisopentylphenyl, Ar = 2,6-$Dipp_2$-C_6H_3).

selectively afford P_4-butterfly complexes [(^{Dipp}BDI)Mg(THF)$_x$-Fp(μ-P_4)] (**3**: $x = 0$; **3-THF**: $x = 1$) and [(^{Dipp}BDI)MgFp*(μ-P_4)] (**4**). The reversible nature and the mechanism of the P_4 activation reaction are investigated using variable-temperature ^{31}P NMR spectroscopy, ^{1}H exchange NMR spectroscopy, and DFT calculations. An analysis of the non-covalent interactions highlights the essential role of the magnesium cation in stabilizing the complexes. Thermolysis or photolysis of **3-THF** and **4** generate rare tetraphosphacyclopentadienolate transition metal complexes **7** and **8**. Additionally, we show that 'P_4-butterfly' ligand in **4** is readily functionalized with various electrophiles. These reactions afford unprecedented mixed-substituted bicyclo[1.1.0]tetraphosphabutanes of type Fp*P_4R [**9–13**, R = C(N^{i}Pr)$_2$ (**9**), BPh_2 (**10**), $SnPh_3$ (**11**), $Si(SiMe_3)_3$ (**12**), $PMes_2$ (**13**)] as well as the octaphosphane [$Ar_2Sn_2P_8Fp^*_2$] (**14**, Ar = 2,6-$Dipp_2$-C_6H_3). Our results demonstrate that inorganic Grignard reagents act as effective metal-based Lewis pairs, enabling the selective activation of P_4 and the targeted functionalization of the resulting P_4^{2-} ligand.

Results and discussion

Synthesis and characterization of P_4-butterfly complexes

Inspired by the work of Crimmin and Mountford on the use of the inorganic Grignard reagents **1** and **1-THF** in C–F activation and heterocumulene insertion,[14,15] we investigated their reactivity with P_4. Initial ^{31}P NMR spectroscopic studies showed that P_4 readily inserts into the Mg–Fe bond of **1-THF** in THF-d_8 or C_6D_6 to generate **3-THF**, which gives rise to an AMX_2 spin system. Likewise, the reaction of **1** with P_4 in toluene-d_8 afforded the THF-free analogue **3**. Complexes **3** and **3-THF** can be isolated as air-sensitive yellow-orange crystals in moderate yields (50% and 22%, respectively). The AMX_2 spin systems

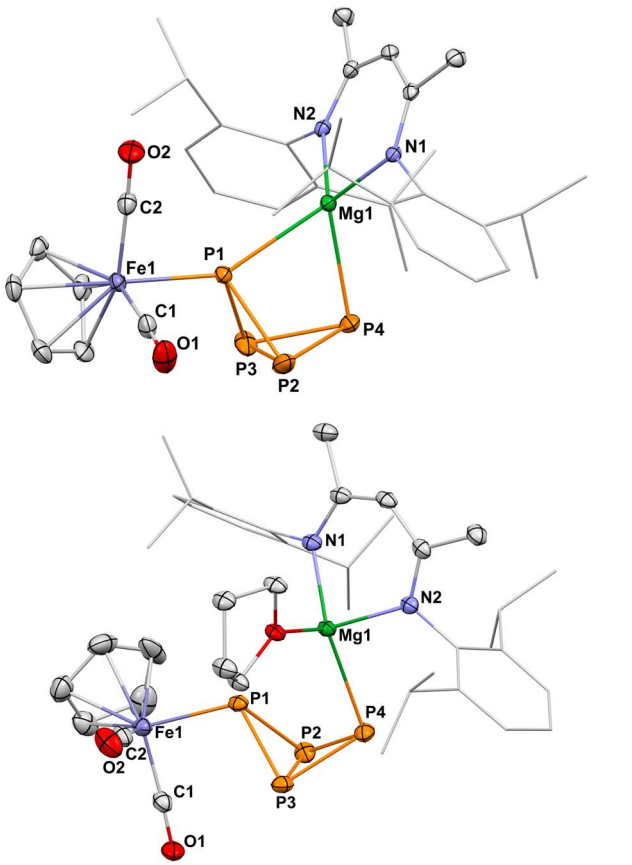

Fig. 2 Solid-state molecular structures of **3** (top) and **3-THF** (bottom) measured at 123 K. Displacement ellipsoids are shown at the 30% probability level. Hydrogen atoms, non-coordinating solvent molecules and disordered groups are omitted for clarity. Selected bond lengths [Å] and angles [°] of **3**: Fe1–P1 2.3023(6), Mg1–P4 2.5623(8), Mg1–P1 2.6529(8), P1–P2 2.2188(7), P1–P3 2.2247(7), P2–P3 2.163(1), P2–P4 2.1922(9), P3–P4 2.1956(8), C1–O1 1.144(3),C2–O2 1.143(3), P1–Mg1–P4 70.55(2), N1–Mg1–N2 92.64(7). **3-THF**: Fe1–P1 2.3527(6), Mg1–P4 2.6320(8), Mg1–P1 2.9427(8), P1–P2 2.2044(7), P1–P3 2.2112(8), P2–P3 2.1598(8), P2–P4 2.2034(8), P3–P4 2.1909(8), C1–O1 1.156(3), C2–O2 1.147(3), P1–Mg1–P4 63.44(2), N1–Mg1–N2 92.16(7).

observed in the ^{31}P NMR indicate the formation of a P_4-butterfly structure. The $^2J_{31P-31P}$ coupling constants between the wingtip P atoms (47.0 and 36.8 Hz) indicate an *endo*,*exo* configuration of the butterfly-P_4 ligands,[10,12,19] suggesting that there is no through-space interaction between these P atoms.[20] The ^{1}H and ^{31}P NMR spectra furthermore indicate that **3** and **3-THF** are in an equilibrium with the starting materials **1** and **1-THF** and P_4 in deuterated benzene and deuterated THF (*vide infra*).

Single-crystal X-ray diffraction (scXRD) studies on **3** and **3-THF** confirmed that the P_4 molecule has formally inserted into the Mg–Fe bond (Fig. 2). Both complexes crystallize as the *endo*,*exo* isomer. One of the wing-tip phosphorus atoms (P1) coordinates to iron. In the structure of **3**, the Mg atom bridges the two wing-tip P atoms, P1 and P4, with similar distances (Mg1–P1 2.6529(8) Å, Mg1–P4 2.5623(8) Å). In contrast, a THF molecule is coordinated to the magnesium atom in **3-THF**, resulting in a more asymmetric coordination environment (Mg1–P1 2.9427(8) Å, Mg1–P4 2.6320(8) Å). The P–P bond lengths are characteristic of P_4-butterfly species, revealing a short P–P bond between the bridgehead P atoms (**3**: P2–P3 2.163(1) Å; **3-THF**: P2–P3 2.1598(8) Å).[8,11,19]

To assess the influence of substituents on the Cp ligand, we synthesized the novel [(^{Dipp}BDI)MgFp*] complex **2**.† Unlike **1**, complex **2** forms a dimer in the solid state *via* the coordination of the CO ligands to magnesium, as previously observed for related complexes[9,10].‡ ^{1}H NMR and DOSY NMR studies reveal an equilibrium between monomeric and dimeric species in C_6D_6 solution (see Fig. S71–S73). The reaction of **2** (0.5 equiv.) with P_4 in toluene or benzene cleanly yields **4** as a single *endo*,*exo*-configured product, which can be isolated in a high yield (72%) as a yellow-orange crystalline solid (Scheme 1). The molecular structure is very similar to that of **3**, as determined by scXRD studies (Fig. 2). In contrast, complex **4** forms a mixture of *endo*,*exo* and *exo*,*exo* complexes when using THF. Both isomers decompose rapidly in that solvent to the symmetrical [{Fp*}$_2$(μ-P_4)] (Fig. S83 and S84, SI), illustrating the stabilizing nature of the ion-pairing between the [(^{Dipp}BDI)Mg]$^+$ cations and the [Fp*(μ-P_4)] anion.

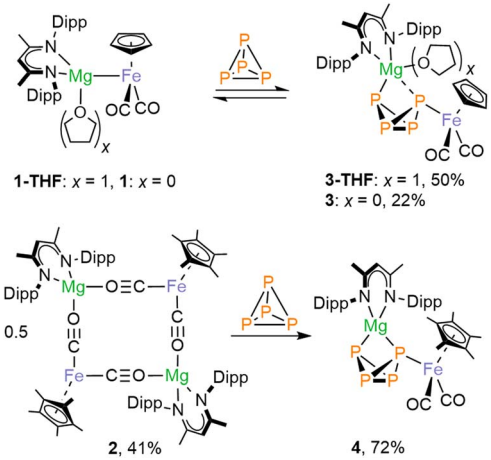

Scheme 1 Synthesis of complexes **3-THF**, **3** and **4**. The reaction is reversible with **1** and **1-THF** and irreversible with **2**.

Mechanism of the P_4 insertion reaction

To gain more insight into the temperature-dependent equilibrium between **1-THF**, **3-THF** and P_4, we performed variable-temperature (VT) ^{31}P{^{1}H} NMR spectroscopic measurements of **3-THF** in THF-d_8. A van 't Hoff analysis provided the thermodynamic parameters of the P_4 activation reaction (ΔG(298 K) = −3.9(±1.7) kJ mol^{-1}, ΔH = −37.8(±0.8) kJ mol^{-1} and ΔS = −115(±3) J mol^{-1} K^{-1}; see also Table S8 and Fig. S63). Exchange spectroscopy (EXSY) of the Cp signals in the ^{1}H NMR spectrum revealed a low activation barrier ($\Delta G^{\ddagger}$(298 K) = 73.1(±4.3) kJ mol^{-1}, $\Delta H^{\ddagger}$ = 16.9(±2.9) kJ mol^{-1}, $\Delta S^{\ddagger}$ (298 K) = −188.3(±10.3) J mol^{-1} K^{-1}; see Table S11 and Fig. S69). **3-THF** shows a similar behaviour in toluene-d_8 (ΔG(298 K) = −5.0(±6.4) kJ mol^{-1}, ΔH = −43.7(±3.1) kJ mol^{-1} and ΔS = −129(±11) J mol^{-1} K^{-1}; see Table S9 and Fig. S63, S64, S76). However, in this case, the van 't Hoff plot shows a nonlinear relationship between 193 K and 233 K, suggesting that the equilibrium was not reached at low temperatures.

The donor-free complex [(^{Dipp}BDI)MgFp] (**3**) shows a similar temperature-dependent equilibrium in non-coordinating solvents (C_6D_6 or toluene-d_8).[15] In toluene-d_8, an additional P-containing species is observed at temperatures below 253 K besides P_4, which we assign to the *exo*,*exo* isomer of **3** (Fig. S79 and S80).

DFT calculations suggest that the mechanism of the P_4 activation reaction in THF-d_8 likely involves the heterolytic cleavage of the Mg–Fe bond in compound **1-THF** (Fig. 3), which appears to be barrierless (see Fig. S128). The coordination of

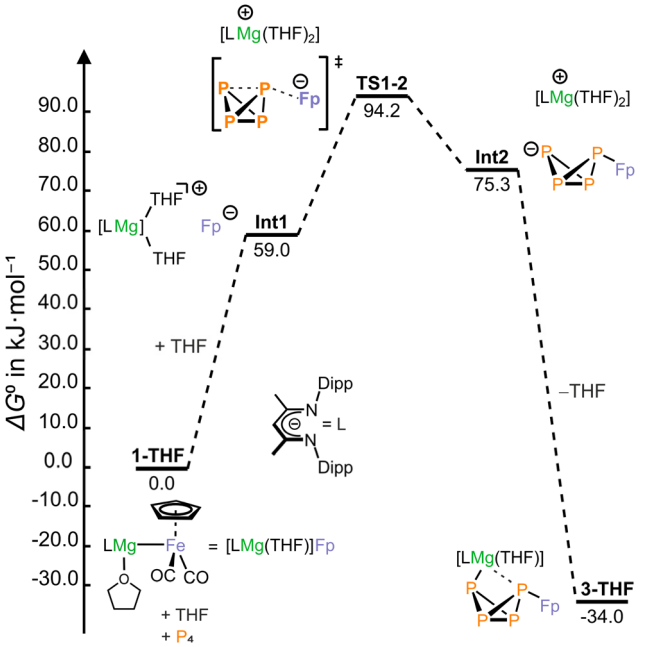

Fig. 3 Computed Gibbs free energy profile for P_4 activation with **1-THF**. Relative Gibbs free energies are presented in kJ mol^{-1}. Level of theory: MN15/def2-TZVP/SMD(THF)//MN15/def2-SVP/SMD(THF).

THF generates a solvent-separated ion pair consisting of the Fp^- anion and the $[(^{Dipp}BDI)Mg(THF)_2]^+$ cation. Fp^- attacks P_4 to form the $[FpP_4]^-$ anion, which is then trapped by $[(^{Dipp}BDI)Mg(THF)_2]^+$. The Gibbs free energy (ΔG^0 and $\Delta G^{\ddagger}$) profile calculated by density functional theory (DFT) for this mechanism shown in Fig. 3 qualitatively agrees with the experimental data. However, the calculations slightly overestimate ΔG^0 and underestimate $\Delta G^{\ddagger}$. In non-coordinating solvents such as toluene, an alternative mechanism to that depicted in Fig. 3 is likely, in which the CO ligands coordinate to magnesium as previously observed in the molecular structures of magnesium-transition metal carbonylates.[9,10] A different reaction pathway, in which P_4 coordinates to Mg, but the $[(^{Dipp}BDI)Mg]^+$ unit does not dissociate from the Fp^- anion, is also feasible and features only a slightly higher activation barrier as shown by DFT calculations (see Fig. S129 in the SI). The coordination of P_4 to magnesium(II) centers has already been reported.[18]

It is noteworthy that the complexes $[(^{Dep}BDI)Mg(THF)Fp]$ (**5-THF**) and $[(^{Mes}BDI)Mg(THF)Fp]$ (**6-THF**), featuring smaller Mes and Dep substituents on the BDI ligand, gave only traces of the desired P_4-butterfly in C_6D_6 (5% and 3%, respectively), according to qualitative integration of the $^{31}P\{^1H\}$ NMR spectra (Dep = 2,6-Et_2-C_6H_3, see Table S15 and Fig. S83). This indicates that the strength of the ion-pairing interaction between the Fp^- and the magnesium ion significantly influences the equilibrium. The DFT-calculated reaction energies are in full agreement with these findings, showing a greater thermodynamic preference for the formation of the P_4-butterfly derivatives with Ar = Dipp by up to −16.2 kJ mol^{-1}, compared to Ar = Dep or Mes (Table S21).

Non-covalent interaction analysis

To investigate the influence of the cation on the thermodynamic stability, we performed a non-covalent interaction (NCI) analysis on the complexes **3**, **4** and the hypothetical complex [LiFp*(μ-P_4)][21].§ The resulting NCI and reduced density gradient (RDG) plots obtained from the wavefunction calculated at the MN15/def2-TZVP/SMD(THF)//MN15/def2-SVP/SMD(THF)[22] level of theory are shown in Fig. 4 (see also Fig. S130–S132). Ionic interactions within compound **4** (see Fig. 4 left) and [LiFp*Fe(μ-P_4)] (see Fig. 4 right) are visualized in green to blue (sign(λ_2)ρ < −0.015 a.u.) in the NCI isosurfaces and RDG scatter plots. The Mg cation in **4** shows a stronger interaction with the wingtip phosphorus atoms compared to the Li cation in [LiFp*(μ-P_4)], as indicated by the dark blue color. Dispersion interactions between the $[(^{Dipp}BDI)Mg]^+$ cation and $[Fp^*(\mu\text{-}P_4)]^-$ additionally stabilize the complex (Fig. 4).

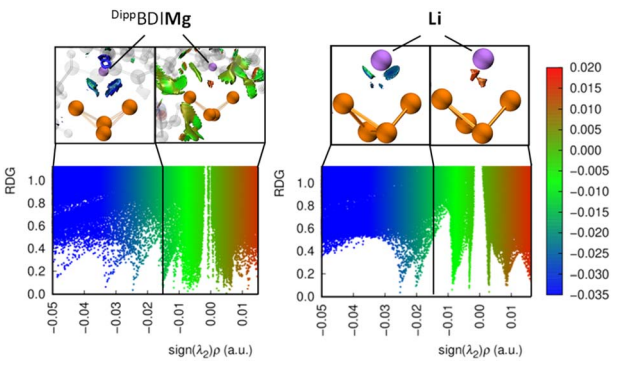

Fig. 4 3D NCI-plot and RDG scatter plot of **4** (left) and of [LiFp*(μ-P_4)] (right). RDG scatter plot and 3D NCI-plots for ionic (sign(λ_2)ρ range: −0.05 a.u. to −0.015 a.u.) and van der Waals region (sign(λ_2)ρ range: −0.015 a.u. to +0.015 a.u.) The repulsive interaction regions were omitted for clarity.

Thermolysis of 3-THF and photolysis of 4: synthesis of 7 and 8

Given the propensity of carbonyl complexes for the dissociation of CO,[23] we examined the thermal and photolytic stability of **3-THF**. Upon heating of a solution in C_6D_6 to 60 °C for 5 d, **3-THF** was converted to a new species **7** (Scheme 2) characterized by an AA′BB′ spin system in the $^{31}P\{^1H\}$ NMR spectrum (δ = 44.3 ppm and 30.7 ppm, Fig. S15 and Table S1). It is noteworthy that the presence of the THF ligand in **3-THF** is essential for the formation of **7**, since the THF-free **3** appears to be completely stable in C_6D_6 upon heating to +60 °C and under irradiation with a neutral white-light LED (see Fig. S87). In contrast, **4** is also thermally stable but rearranges upon exposure to daylight, forming complex **8** over several days (Scheme 2).

The $^{31}P\{^1H\}$ NMR spectrum of **8** shows an AA′XX′ spin system similar to that of **7** (δ = 61.3 and 36.4 ppm, see Fig. 5). The scXRD analyses of **7** and **8** revealed the formation of ferrocene-like sandwich complexes with η^5-coordinated tetraphosphacyclopentadienolate ligands. The planar $P_4C(O)$ rings are eclipsed with respect to the co-planar Cp or Cp* moiety. The P–P and P–C bond lengths indicate a delocalized bonding situation (**7**: P–P2.1013(8) to 2.124(1) Å, P–C1.786(2) and 1.790(2) Å; **8**: P–P2.100(2) to 2.135(2) Å, P–C1.781(5) and 1.785(6) Å). Complex **7** crystallizes as a monomer while the THF-free compound **8** forms a polymeric structure *via* coordination of the P2 atom to a $[(^{Dipp}BDI)Mg]^+$ cation of an adjacent molecule (Mg1–P2 2.793(2) Å, Fig. S93). To our knowledge, **7** and **8** are the first complexes featuring η^5-coordinated tetraphosphacyclopentadienolate $P_4C(O)^-$ ligands. A similar CO insertion resulting in an η^3-$P_4C(O)$ ligand has been observed for the reaction of $[Fe_2(CO)_9]$ with $(Cp'''Fe)_2(\mu\text{-}P_4)$ ($Cp''' = C_5H_2{}^tBu_3$), which affords the oligonuclear complex $[\{Cp'''Fe(CO)_2\}_2(\mu_4,\eta^{3:1:1:1}\text{-}P_4CO)\{Fe(CO)_4\}\{Fe(CO)_3\}]$.[24]

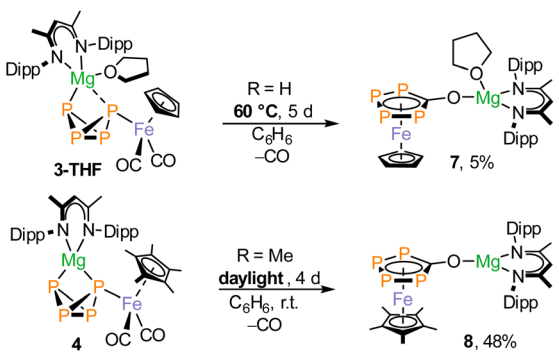

Scheme 2 Synthesis of **7** and **8**, r.t. = room temperature.

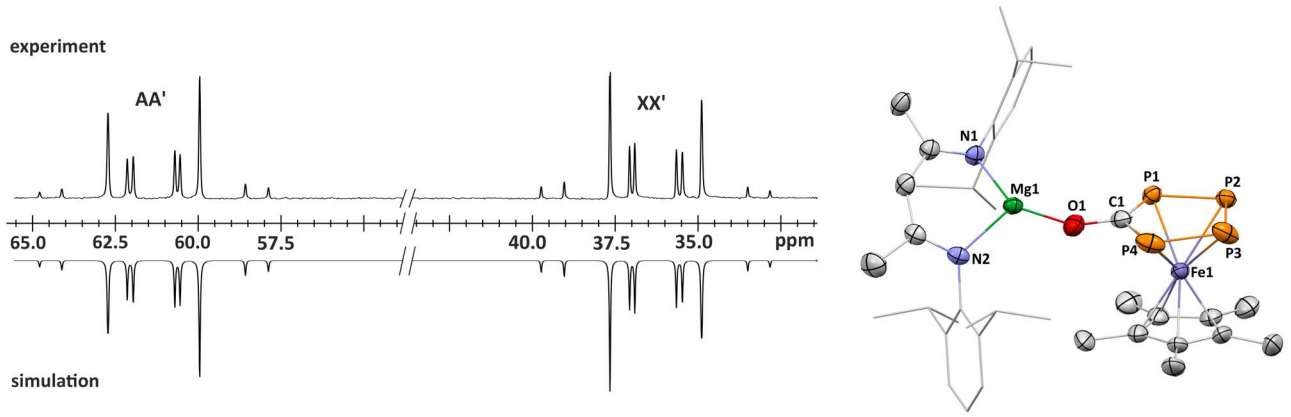

Fig. 5 Experimental (upwards) and simulated (downwards) $^{31}P\{^1H\}$ NMR spectrum of **7** (left) and its solid-state molecular structure measured at 123 K (right). The solid-state molecular structure and the $^{31}P\{^1H\}$ NMR spectrum of **8** are similar and therefore displayed in the ESI. Displacement ellipsoids are shown at the 30% probability level. Hydrogen atoms are omitted, and the Dipp groups are shown in wireframe representation for clarity. Selected bond length [Å] and angles [°]: P3–P4 2.100(2), P1–P2 2.112(2), P2–P3 2.135(2), P1–C1 1.781(5), P4–C1 1.785(6), C1–O1 1.309(5), Fe–P 2.345(1)–2.361(2), Fe1–C1 2.231(4), C1–O1–Mg1 145.8(3), $P_4C_{centroid}$–Fe1–$C_{5\text{-}centroid}$ 174.1.

Additionally, a few related tetraphospholide complexes are known which display similar P–P bond lengths,[25–29] *e.g.* $[Cp^RFe(\eta^5\text{-}P_4CR')]$ (Cp^R = Cp, R′ = ^{t}Bu, adamantyl, $SiMe_3$; Cp^R = Cp*, R′ = Mes, phenyl; Cp^R = Cp‴, R′ = ^{t}Bu),[25,29] and $[Cp^*Fe(P_4SiL)]$ (L = $PhC\{N^tBu\}_2$).[26]

Reactivity of 4 towards electrophiles

The high-yielding synthesis of complex **4** enabled us to investigate its reactivity towards electrophiles in detail. During these studies, we found that **4** reacts readily and selectively with numerous electrophiles, including main-group element halides and heterocumulenes (Scheme 3). The products exhibit characteristic AMX_2 spin systems in the $^{31}P\{^1H\}$ NMR spectra, which provide evidence for P-functionalized P_4-butterfly compounds. Using bulky electrophiles such as ^{i}PrNCN^{i}Pr, Ph_2BCl, Ph_3SnCl, $(Me_3Si)_3SiCl$, and Mes_2PCl we were able to isolate the new P_4-butterfly complexes **9–13**. Complexes **9**, **10** and **12** are stable in solution for several days, while **11** and **13** gradually decompose at ambient temperature (Fig. S54 and S84). It is noteworthy that **11** dimerises slowly to a tricyclic P_8 cluster **15**, as revealed by ^{31}P NMR data and a preliminary scXRD analysis (Fig. S48). Weigand and co-workers observed a similar dimerization reaction for the pentaphosphane $P_5(C_6F_5)_2$ generated from $(^{Dipp}BDI)GaP_4$ butterfly with $(C_6F_5)_2PBr$.[30]

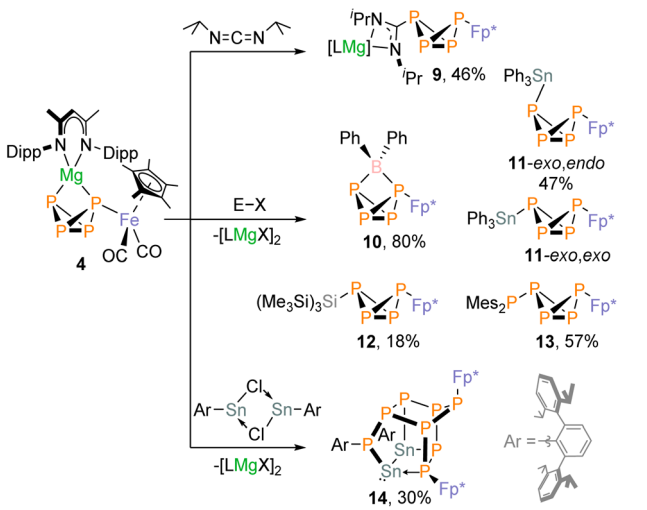

Scheme 3 Reactivity of **4** towards selected electrophiles.

ScXRD studies revealed the molecular structures of **9–13**. Complex **9** results from an insertion of the carbodiimide ^{i}PrNCN^{i}Pr into the Mg–P bond of **4**. The two nitrogen atoms coordinate to magnesium, and the carbon atom is bound to phosphorus (Fig. 6). For **9**, **12**, and **13** (Fig. S1), the butterfly-P_4 unit is an *exo*,*exo* configuration with the Fp* and carbodiimide, $(Me_3Si)_3Si$- and Mes_2P-substituents pointing toward the bridgehead P atoms. In contrast, complex **10** shows a symmetrically bridging Ph_2B moiety (P–B 2.016(2) Å and 2.055(2) Å). An *endo*,*exo* configuration is likewise observed for the Ph_3Sn-substituted complex **11**.

The $^{31}P\{^1H\}$ NMR data are consistent with these crystallographic findings. For complex **9**, the $^2J_{31P-31P}$ coupling (258 Hz) is larger than the $^1J_{PP}$ couplings (179 Hz, 185 Hz), indicating an *exo*,*exo* butterfly structure in solution. The $^{13}C\{^1H\}$ NMR spectrum displays a doublet of doublet for the quaternary carbon atom of the carbodiimide unit due to C–P coupling (δ = 175.0 ppm, $^1J_{PC}$ = 103.9 Hz, $^3J_{PC}$ = 23.3 Hz, Fig. S21). The *exo*,*exo* isomer is also present for **12** and **13**, as evidenced by the high-field shifted P_M resonances of the AMX_2 spin systems and large $^2J_{PP}$ couplings ($^2J_{AM}$ = 235 Hz and 259 Hz, respectively; see Tables S5 and S6), which result from through-space interactions of the lone pairs.[10] Additionally, ^{29}Si satellites ($^1J_{SiP}$ = 97.5 Hz) were detected for the P atom with the $(Me_3Si)_3Si$ substituent. In contrast, the small $^2J_{PP}$ coupling constant ($^2J_{AM}$ = 33 Hz) indicates that compound **10** retains the *endo*,*exo* configuration in solution. The resonances assigned to the wingtip phosphorus atoms P1 and P4 exhibit chemical shifts similar to compound **4**, while the signal of the bridgehead phosphorus atoms P2 and P3 is shifted downfield by 50.4 ppm. The $^{11}B\{^1H\}$ NMR spectrum shows a broad signal ($\Delta\nu_{\frac{1}{2}}$ = 362 Hz) at 20.5 ppm with

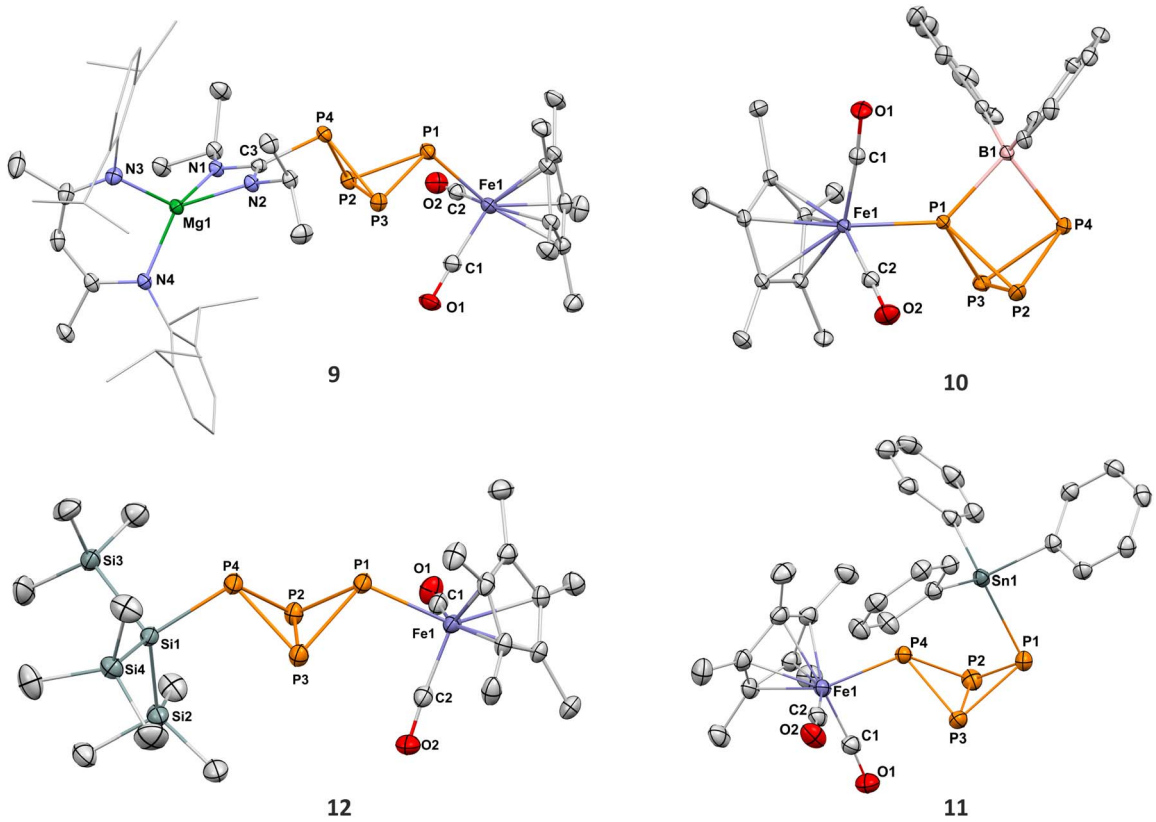

Fig. 6 Solid-state molecular structures of **9**, **10**, **11** and **12** measured at 123 K. Displacement ellipsoids are shown at the 30% probability level. Hydrogen atoms, non-coordinating solvent molecules and disordered groups are omitted for clarity. The Dipp groups in **7** are depicted in wireframe representation for clarity. Selected bond length[Å] and angles [°] are for **9**: Fe1–P1 2.3064(6), P1–P2 2.2169(6), P1–P3 2.2286(7), P2–P3 2.1795(7) P2–P4 2.2119(7), P3–P4 2.2083(7), P4–C3 1.889(2), C1–O1 1.148(2), C2–O2 1.147(2), N2–C3 1.332(2), N1–C3 1.335(2), N1–C3–N2 114.4(2), N3–Mg1–N4 94.24(7). **10**: Fe1–P1 2.2434(4), P1–B1 2.016(2), P4–B1 2.055(2), P1–P2 2.2063(6), P1–P3 2.2035(5), P2–P3 2.1974(7), P3–P4 2.2100(6), P2–P4 2.2108(7), C1–O1 1.145(2), C2–O2 1.142(2), P1–B1–P4 83.67(7), Fe1–P1–B1 134.90(5). **11**: Fe1–P4 2.2734(7), Sn1–P1 2.5675(7), P1–P2 2.2063(9), P1–P3 2.2080(9), P2–P3 2.179(1), P2–P4 2.2233(9), P3–P4 2.2060(9), C1–O1 1.147(3), C2–O2 1.149(3). Second molecule in asymmetric unit: Fe1–P4 2.2848(7), Sn1–P1 2.5549(7), P1–P2 2.206(1), P1–P3 2.208(1), P2–P4 2.2261(9), P3–P4 2.2084(9), C1–O1 1.145(3), C2–O2 1.145(3). **12**: Fe1–P1 2.294(1), P4–Si 2.294(1), P1–P2 2.218(1), P1–P3 2.231(2), P3–P4 2.217(1), P2–P3 2.167(1), P2–P4 2.214(1), C1–O1 1.152(5), C2–O2 1.144(5), Si1–P4–P3 101.91(5), P1–P3–P4 81.98(5), Fe1–P1–P3 109.49(5).

unresolved coupling to phosphorus. The $^{31}P\{^1H\}$ NMR spectra of the Ph_3Sn-substituted complex **11** display two distinct AMX_2 spin systems in an approximate 1 : 1 integral ratio, indicating that the *endo*,*exo* and *exo*,*exo* isomers coexist in solution (Fig. S30). However, when a sample of isolated **11** was dissolved at −80 °C in toluene-d_8 and the $^{31}P\{^1H\}$ NMR was recorded at −80 °C, only the signals of the *endo*,*exo* isomer were observed ($^2J_{AM}$ = 16 Hz, Table S3). Variable-temperature $^{31}P\{^1H\}$ NMR spectroscopy of **11** shows a slow conversion to an equilibrium mixture of the *endo*,*exo* and *exo*,*exo* isomer at elevated temperature (Fig. S81). The ^{119}Sn NMR spectrum of *endo*,*exo* **11** dissolved at −80 °C shows a doublet of doublets with a $^1J_{119Sn-31P}$ coupling of 973 Hz and a smaller coupling of $^1J_{119Sn-31P}$ = 299 Hz in agreement with the $^{117/119}Sn$–P coupling constants derived from the $^{31}P\{^1H\}$ NMR spectrum (see Table S3).

The reactivity of **4** towards electrophiles strongly depends on the nature and steric bulk of the electrophile. The substituents must provide sufficient steric protection to stabilize the resulting butterfly complex without suppressing reactivity. Thus, $^{31}P\{^1H\}$ NMR spectroscopic monitoring studies indicate that **4** cleanly reacts with the moderately bulky electrophile Me_3SiBr to afford the desired P_4-butterfly compound Fp^*P_4-$SiMe_3$. However, this compound is unstable and decomposes overnight at room temperature. In contrast, the reaction of the bulkier ^{t}BuMe$_2$SiCl with **4** is slow, resulting in an incomplete substitution reaction. Oxidizing electrophiles such as (2,6-Mes$_2$-C_6H_3)PCl_2 (Mes = C_6H_2-2,4,6-Me_3) produce $Fp^*_2P_4$ and P_4 among other decomposition products.

The reaction of **4** with $[ArSnCl]_2$ (0.5 equiv., Ar = 2,6-Dipp$_2$-C_6H_3, Dipp = 2,6-^{i}Pr$_2$-C_6H_3) affords the polycyclic compound **14** (Fig. 7a), which formally is the dimerization product of the expected P_4-butterfly species Fp^*P_4SnAr. The molecular structure of **14** consists of a pentacyclo[5.2.1.0^{2,6}.0^{3,9}.0^{4,8}]decane-like P_8Sn_2 core derived from a norbornane-like P_7 moiety with an exocyclic ArP unit and a Sn–Sn single bond (2.8591(2) Å).[31] The P–P bond lengths (2.1747(6)–2.2483(6) Å) are in the range of P–P single bonds. Notably, the Sn1–P1 bond length 2.6726(4) Å results from a dative interaction involving the lone pair of P1.

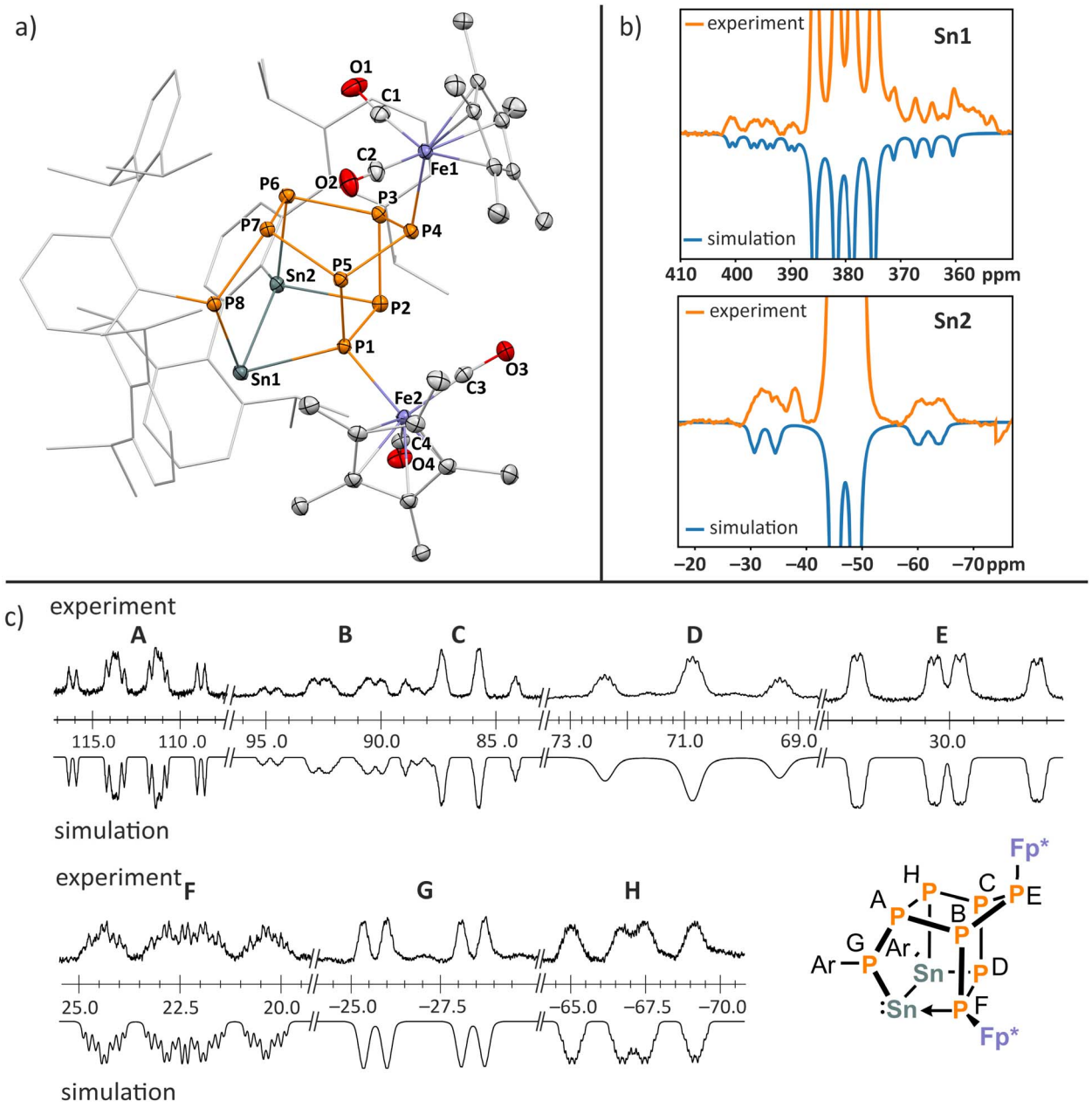

Fig. 7 (a) Solid-state molecular structure of **14** measured at 123 K. Displacement ellipsoids are shown at the 30% probability level. Hydrogen atoms are omitted and Ar-groups are represented as wireframe for clarity. Selected bond length [Å] and angles [°]: Sn1–Sn2 2.8591(2), Sn1–P1 2.6726(4), Sn1–P8 2.5967(4), Sn2–P2 2.5968(4), Sn2–P6 2.5707(4), P1–P2 2.2644(6), P1–P5 2.2191(6), P2–P3 2.2015(6), P3–P4 2.1950(6), P3–P6 2.2483(6), P4–P5 2.1747(6), P5–P7 2.2054(6), P6–P7 2.2337(6), P7–P8 2.2008(6), Sn1–Sn2–P2 89.673(10)), P1–Sn1–Sn2 74.309(9), P6–Sn2–Sn1 106.62(1). (b) $^{119}Sn\{^{1}H\}$ experimental NMR spectrum (224 MHz, 298 K, C_6D_6) (top) and simulation (bottom). An exponential window function (WDW EM) with a line broadening of 50 Hz has been used. The baseline has been corrected using a multipoint spline with the ".basl" and "sab" commands in Bruker TopSpin 4.20. (c) $^{31}P\{^{1}H\}$ experimental spectrum (162 MHz, 298 K, C_6D_6) (top) and simulation bottom.

The remaining Sn–P distances are in a close range (2.5707(4)–2.5967(4) Å), consistent with Sn–P single bonds. The structural framework of **14** is reminiscent of bishomocubanes derived from dimethyl dicyclopentadienedicarboxylate (Thiele's ester).[32] Additionally, some related carbocyclic polyphosphanes have been described, resulting from the dimerization of 1,2,4-triphosphacyclopenta-1,3-dienes or the reaction of R_3Sn stabilized 1,2,4-triphosphacyclopenta-1,3-dienes with *tert*-butylphosphaalkyne.[33] Notably, the dimerization of the As_4-butterfly complexes $[\{Cp'''Fe(CO)_2\}_2(\mu,\eta^{1:1}\text{-}As_4)]$ or $[\{Cp^*Cr(CO)_3\}_2(\mu,\eta^{1:1}\text{-}As_4)]$ afford realgar-like (tricyclo [3.3.0.0^{3,7}]octane)-As_8 species.[34] Similar realgar-like P_8 units are also known.[35]

The ^{119}Sn NMR spectrum of **14** shows an apparent doublet of doublets at 380 ppm, and a broad doublet ($\Delta\nu_{\frac{1}{2}} > 700$ Hz) with unresolved fine structure at −47 ppm. The assignment of the Sn1 and Sn2 signals is based on the calculated $^{1}J_{119Sn-31P}$ coupling constants of 1471 Hz for Sn1–P8, 970 Hz for Sn1–P1

and 823 Hz for Sn2–P6 (Fig. 7b; see SI, section 8.3 for details). These data compare well with the experimental values of 1540 Hz, 882 Hz and 830 Hz, respectively. The ^{117}Sn and ^{119}Sn satellites could be detected in the ^{119}Sn NMR spectrum ($^{1}J_{119Sn1-119Sn2} \approx 6700$ Hz; calculated −7663 Hz), confirming that the Sn–Sn bond remains intact in solution. For comparison, the $^{1}J_{119Sn-119Sn}$ coupling constants in Ar*SnSnPh$_2$Ar* and Ar*SnSn(Me$_2$)Ar* [Ar* = 2,6-(2,4,6-^{i}Pr$_3$-C$_6$H$_2$)$_2$-C$_6$H$_3$] are 7237 Hz and 8330 Hz, respectively.[36]

The ^{31}P{^{1}H} NMR spectrum of **14** displays a set of eight multiplets between 112.4 ppm and −67.1 ppm for the eight distinct P-atoms. The coupling constants were determined by simulating the spectrum using an iterative fitting procedure (Fig. 7c and Table S7, SI). Compound **14** is unstable in solution at ambient temperature. Upon storing a solution at room temperature, the signals of **14** gradually disappear over the course of three weeks, and two new sets of signals appear in the ^{31}P{^{1}H} NMR spectrum in the same chemical shift range as for **14**, indicating that it rearranges slowly in solution to form a new complex **16** (see SI, Fig. S60). A preliminary scXRD analysis shows that **14** eliminates one CO ligand. As a result, one of the Fe atoms binds to two adjacent phosphorus atoms (Fig. S49). Based on the very similar chemical shifts and coupling constants in the ^{119}Sn and ^{31}P{^{1}H} NMR spectra (Fig. S57 and S60), we assume that two isomers of **16** coexist in solution.

Conclusions

We have shown that the inorganic Grignard reagents **1** and **2** effectively activate P$_4$ through furnishing P$_4$-butterfly dianions that are coordinated by Fe and the bulky *β*-diketiminato magnesium cation [(^{Dipp}BDI)Mg]$^+$. Our theoretical analysis emphasizes the importance of non-covalent and dispersion interactions in stabilizing these complexes, which appear to be stronger for [(^{Dipp}BDI)Mg]$^+$ than for Li$^+$.§ The reversible dissociation of the Fe–Mg Lewis pairs **1** and **2** into solvent-separated ion pairs appears to be key. According to DFT calculations, the reactions proceed stepwise *via* nucleophilic attack by the Fp$^-$ or Fp*$^-$ anion on P$_4$ and subsequent coordination to [^{Dipp}BDIMg]$^+$. However, unlike previous studies, these reactions do not require an external Lewis acid, simplifying reactivity investigations. Reactions of **4** with electrophiles generate a variety of new mixed substituted P$_4$-butterfly species **9–13**, as well as the novel Sn$_2$P$_8$ cluster **14**. Additionally, thermally or photochemically induced rearrangements led to rare tetraphosphole complexes **7** and **8**.

Our results indicate that combining transition-metalate anions with the [^{Dipp}BDIMg]$^+$ cation is a promising strategy for deliberate and selective P$_4$ activation and functionalization. When sufficient steric bulk is provided, the resulting P$_4$-butterfly complexes can be easily isolated, marking an ideal starting point for future reactivity studies. In other cases, dimerization to P$_8$ frameworks can be observed. Ongoing work in our group focuses on the reaction chemistry of complexes **9–14** and on the broader applicability of our approach using a wider range of metal-based Lewis pairs.

Author contributions

F. G. conceptualisation, investigation – synthesis and characterisation, writing – original draft; J. B. investigation – DFT studies of the mechanism and NCI analysis; W. M. S. investigation – DOSY and EXSY studies; F. W. investigation – Sn NMR studies and DFT calculations; R. W., G. B. conceptualisation, supervision; R.W., R. G., H. Z. supervision and funding acquisition. All authors contributed to manuscript review, editing and discussion.

Conflicts of interest

There are no conflicts to declare.

Data availability

CCDC 2529860–2529874 and 2541029 contain the supplementary crystallographic data for this paper.[38a–p]

The data supporting the findings of this work is available in the main text or the electronic supplementary information (SI). Primary research data for this work is openly accessible on Radar4Chem (https://radar4chem.radar-service.eu/radar/de/home) under the DOI: https://doi.org/10.22000/7wa7f1kdq20s260j. Supplementary information: experimental procedures, details of NMR spectroscopic studies, scXRD data, cyclic voltammetry data, IR and UV-vis spectra, and computational data. See DOI: https://doi.org/10.1039/d6sc01229a.

Acknowledgements

We thank the Deutsche Forschungsgemeinschaft for funding (RTG 2620 Ion Pair Effects in Molecular Reactivity, project number 426795949). J. B. and H. Z. acknowledge the computational and data resources provided by the Leibniz Supercomputing Centre (https://www.lrz.de). F. G. thanks the Fonds der Chemischen Industrie for a Kekulé Fellowship.

Notes and references

† The Fp*$^-$ anion in **2** is more electron-rich, which should favour the insertion product as demonstrated for the reaction of KFp* with CO$_2$.[37]

‡ Complex **2** forms an Mg–OC–Fe bonded monomer upon crystallization from DME (Fig. S103) and a dimer with similar Mg–OC–Fe linkages upon crystallization from toluene (Fig. S101). Additionally, monomeric Mg–Fe-bonded structures have been obtained for **5-THF** and **6-THF** by crystallization from THF (Fig. S99 and S100). In line with previous results by Mountford and co-workers, these data indicate that the aggregation is reversible, depending on the solvent and the crystallization conditions.[14]

§ Lammertsma and co-workers have demonstrated that the reaction of LiFp* and P$_4$ in THF affords a mixture of iron polyphosphides.[12]

1 (*a*) D. Corbridge, *Phosphorus. Chemistry, Biochemistry and Technology, Sixth Edition*, CRC Press, 2013; (*b*) M. A. de Boer, L. Wolzak and J. C. Slootweg in *Phosphorus Recovery and Recycling*, ed. H. Ohtake and S. Tsuneda, Springer

Singapore, Singapore, 2019, pp. 75–100; (*c*) N. Weferling, S. M. Zhang and C. H. Chiang, *Procedia Eng.*, 2016, **138**, 291.

2 (*a*) S. Hauer, T. M. Horsley Downie, G. Balázs, K. Schwedtmann, J. J. Weigand and R. Wolf, *Angew. Chem., Int. Ed.*, 2024, **63**, e202317170; (*b*) F. Dielmann, M. Elsayed Moussa, C. Riesinger and M. Scheer, *Z. Anorg. Allg. Chem.*, 2024, 650; (*c*) S. Reichl, E. Mädl, F. Riedlberger, M. Piesch, G. Balázs, M. Seidl and M. Scheer, *Nat. Commun.*, 2021, **12**, 5774; (*d*) S. Reichl, F. Riedlberger, M. Piesch, G. Balázs, M. Seidl and M. Scheer, *Chem. Sci.*, 2023, **14**, 7285; (*e*) M. Peruzzini, L. Gonsalvi and A. Romerosa, *Chem. Soc. Rev.*, 2005, **34**, 1038; (*f*) B. M. Cossairt, N. A. Piro and C. C. Cummins, *Chem. Rev.*, 2010, **110**, 4164; (*g*) M. Caporali, L. Gonsalvi, A. Rossin and M. Peruzzini, *Chem. Rev.*, 2010, **110**, 4178; (*h*) C. M. Hoidn, D. J. Scott and R. Wolf, *Chem. Eur J.*, 2021, **27**, 1886; (*i*) L. Giusti, V. R. Landaeta, M. Vanni, J. A. Kelly, R. Wolf and M. Caporali, *Coord. Chem. Rev.*, 2021, **441**, 213927; (*j*) K. Trabitsch, S. Hauer, K. Schwedtmann, P. Royla, J. J. Weigand and R. Wolf, *Inorg. Chem. Front.*, 2025, **12**, 2013; (*k*) M. Scheer, G. Balázs and A. Seitz, *Chem. Rev.*, 2010, **110**, 4236.

3 (*a*) O. J. Scherer, G. Schwarz and G. Wolmershäuser, *Z. Anorg. Allg. Chem.*, 1996, **622**, 951; (*b*) S. Pelties, D. Herrmann, B. de Bruin, F. Hartl and R. Wolf, *Chem. Commun.*, 2014, **50**, 7014; (*c*) D. W. Agnew, C. E. Moore, A. L. Rheingold and J. S. Figueroa, *Angew. Chem., Int. Ed.*, 2015, **54**, 12673; (*d*) M. J. Drance, S. Wang, M. Gembicky, A. L. Rheingold and J. S. Figueroa, *Organometallics*, 2020, **39**, 3394; (*e*) M. Haimerl, C. Graßl, M. Seidl, M. Piesch and M. Scheer, *Chem. Eur J.*, 2021, **27**, 18129; (*f*) S. Heinl, S. Reisinger, C. Schwarzmaier, M. Bodensteiner and M. Scheer, *Angew. Chem., Int. Ed.*, 2014, **53**, 7639; (*g*) R. J. Schwamm, M. Lein, M. P. Coles and C. M. Fitchett, *Angew. Chem., Int. Ed.*, 2016, **55**, 14798; (*h*) J. Haberstroh, C. Taube, J. Fidelius, S. Schulz, N. Israel, E. Dmitrieva, R. M. Gomila, A. Frontera, R. Wolf, K. Schwedtmann and J. J. Weigand, *Chem. Commun.*, 2024, **60**, 8537; (*i*) I. Kovács, G. Baum, G. Fritz, D. Fenske, N. Wiberg, H. Schuster and K. Karaghiosoff, *Z. Anorg. Allg. Chem.*, 1993, **619**, 453; (*j*) S. Khan, R. Michel, J. M. Dieterich, R. A. Mata, H. W. Roesky, J.-P. Demers, A. Lange and D. Stalke, *J. Am. Chem. Soc.*, 2011, **133**, 17889.

4 (*a*) Y. Xiong, S. Yao, M. Brym and M. Driess, *Angew. Chem., Int. Ed.*, 2007, **46**, 4511; (*b*) J. W. Dube, C. M. E. Graham, C. L. B. Macdonald, Z. D. Brown, P. P. Power and P. J. Ragogna, *Chem. Eur J.*, 2014, **20**, 6739; (*c*) C. M. E. Graham, C. L. B. Macdonald, P. P. Power, Z. D. Brown and P. J. Ragogna, *Inorg. Chem.*, 2017, **56**, 9111; (*d*) G. Prabusankar, A. Doddi, C. Gemel, M. Winter and R. A. Fischer, *Inorg. Chem.*, 2010, **49**, 7976; (*e*) D. Reiter, P. Frisch, D. Wendel, F. M. Hörmann and S. Inoue, *Dalton Trans.*, 2020, **49**, 7060; (*f*) M. M. D. Roy, A. Heilmann, M. A. Ellwanger and S. Aldridge, *Angew. Chem., Int. Ed.*, 2021, **60**, 26550; (*g*) D. Sarkar, C. Weetman, D. Munz and S. Inoue, *Angew. Chem., Int. Ed.*, 2021, **60**, 3519; (*h*) P. Dabringhaus, T. Heizmann and I. Krossing, *Chem. Eur J.*, 2023, **29**, e202302212; (*i*) D. Holschumacher, T. Bannenberg, K. Ibrom, C. G. Daniliuc, P. G. Jones and M. Tamm, *Dalton Trans.*, 2010, **39**, 10590; (*j*) J. J. Weigand, M. Holthausen and R. Fröhlich, *Angew. Chem., Int. Ed.*, 2009, **48**, 295.

5 M. Baudler, C. Adamek, S. Opiela, H. Budzikiewicz and D. Ouzounis, *Angew. Chem., Int. Ed.*, 1988, **27**, 1059.

6 (*a*) M. M. Rauhut and A. M. Semsel, *J. Org. Chem.*, 1963, **28**, 471; (*b*) M. M. Rauhut and A. M. Semsel, *J. Org. Chem.*, 1963, **28**, 473; (*c*) M. M. Rauhut, R. Bernheimer and A. M. Semsel, *J. Org. Chem.*, 1963, **28**, 478.

7 K. X. Bhattacharyya, S. Dreyfuss, N. Saffon-Merceron and N. Mézailles, *Chem. Commun.*, 2016, **52**, 5179.

8 J. E. Borger, A. W. Ehlers, M. Lutz, J. C. Slootweg and K. Lammertsma, *Angew. Chem., Int. Ed.*, 2014, **53**, 12836.

9 J. E. Borger, M. S. Bakker, A. W. Ehlers, M. Lutz, J. C. Slootweg and K. Lammertsma, *Chem. Commun.*, 2016, **52**, 3284.

10 J. E. Borger, A. W. Ehlers, M. Lutz, J. C. Slootweg and K. Lammertsma, *Angew. Chem., Int. Ed.*, 2017, **56**, 285.

11 J. E. Borger, A. W. Ehlers, M. Lutz, J. C. Slootweg and K. Lammertsma, *Angew. Chem., Int. Ed.*, 2016, **55**, 613.

12 J. E. Borger, M. K. Jongkind, A. W. Ehlers, M. Lutz, J. C. Slootweg and K. Lammertsma, *ChemistryOpen*, 2017, **6**, 350.

13 (*a*) C. G. P. Ziegler, T. M. Maier, S. Pelties, C. Taube, F. Hennersdorf, A. W. Ehlers, J. J. Weigand and R. Wolf, *Chem. Sci.*, 2019, **10**, 1302; (*b*) C. G. P. Ziegler, C. Taube, J. A. Kelly, G. Hierlmeier, M. Uttendorfer, J. J. Weigand and R. Wolf, *Chem. Commun.*, 2020, **56**, 14071; (*c*) Y. Liu, F. F. Westermair, I. Becker, S. Hauer, M. Bodensteiner, C. Hennig, G. Balázs, F. Meyer, R. M. Gschwind and R. Wolf, *J. Am. Chem. Soc.*, 2025, **147**, 7083; (*d*) M. D. Fritz, J. A. Kelly, G. Balázs and R. Wolf, *ChemistryEurope*, 2026, **4**, e202500257.

14 M. P. Blake, N. Kaltsoyannis and P. Mountford, *Chem. Commun.*, 2013, **49**, 3315.

15 M. Garçon, C. Bakewell, A. J. P. White and M. R. Crimmin, *Chem. Commun.*, 2019, **55**, 1805.

16 (*a*) H. Felkin, P. J. Knowles, B. Meunier, A. Mitschler, L. Ricard and R. Weiss, *J. Chem. Soc., Chem. Commun.*, 1974, 44; (*b*) J. A. Kelly, J. Gramüller, R. M. Gschwind and R. Wolf, *Dalton Trans.*, 2021, **50**, 13985; (*c*) M. Gawron, F. Gilch, D. Schmidhuber, J. A. Kelly, T. M. Horsley Downie, A. Jacobi von Wangelin, J. Rehbein and R. Wolf, *Angew. Chem., Int. Ed.*, 2024, **63**, e202315381; (*d*) V. R. Landaeta, T. M. Horsley Downie and R. Wolf, *Chem. Rev.*, 2024, **124**, 1323.

17 (*a*) M. Arrowsmith, M. S. Hill, A. L. Johnson, G. Kociok-Köhn and M. F. Mahon, *Angew. Chem., Int. Ed.*, 2015, **54**, 7882; (*b*) S. Thum, O. P. E. Townrow, J. Langer and S. Harder, *Chem. Sci.*, 2025, **16**, 4528.

18 M. J. Evans, D. T. Nguyen, J. M. Parr, J. Mullins, R. Mondal, T. Rajeshkumar, L. Maron and C. Jones, *Chem*, 2025, 102650.

19 J. Bresien, K. Faust, C. Hering-Junghans, J. Rothe, A. Schulz and A. Villinger, *Dalton Trans.*, 2016, **45**, 1998.

20 D. C. Meier, Á. García-Romero, D. González-Pinardo, N. H. Rees, A. Lovstedt, I. Fernández and J. M. Goicoechea, *Chem. Sci.*, 2025, **17**, 544.
21 J. Contreras-García, E. R. Johnson, S. Keinan, R. Chaudret, J.-P. Piquemal, D. N. Beratan and W. Yang, *J. Chem. Theory Comput.*, 2011, **7**, 625.
22 (*a*) H. S. Yu, X. He, S. L. Li and D. G. Truhlar, *Chem. Sci.*, 2016, **7**, 6278; (*b*) F. Weigend and R. Ahlrichs, *Phys. Chem. Chem. Phys.*, 2005, **7**, 3297; (*c*) A. V. Marenich, C. J. Cramer and D. G. Truhlar, *J. Phys. Chem. B*, 2009, **113**, 6378.
23 (*a*) J. J. Turner, M. W. George, M. Poliakoff and R. N. Perutz, *Chem. Soc. Rev.*, 2022, **51**, 5300; (*b*) O. J. Scherer, T. Hilt and G. Wolmershäuser, *Organometallics*, 1998, **17**, 4110; (*c*) O. J. Scherer, T. Brück and G. Wolmershäuser, *Chem. Ber.*, 1988, **121**, 935; (*d*) M. Scheer and U. Becker, *J. Organomet. Chem.*, 1997, **545–546**, 451; (*e*) O. J. Scherer, R. Winter and G. Wolmershäuser, *Z. Anorg. Allg. Chem.*, 1993, **619**, 827; (*f*) C. Eichhorn, O. J. Scherer, T. Sögding and G. Wolmershäuser, *Angew. Chem., Int. Ed.*, 2001, **40**, 2859; (*g*) O. J. Scherer, J. Schwalb, G. Wolmershäuser, W. Kaim and R. Gross, *Angew. Chem., Int. Ed.*, 1986, **25**, 363.
24 R. Grünbauer, C. Schwarzmaier, M. Eberl, G. Balázs and M. Scheer, *Inorg. Chim. Acta*, 2021, **518**, 120234.
25 M. Scheer, S. Deng, O. J. Scherer and M. Sierka, *Angew. Chem., Int. Ed.*, 2005, **44**, 3755.
26 R. Yadav, T. Simler, S. Reichl, B. Goswami, C. Schoo, R. Köppe, M. Scheer and P. W. Roesky, *J. Am. Chem. Soc.*, 2020, **142**, 1190.
27 J. A. Kelly, V. Streitferdt, M. Dimitrova, F. F. Westermair, R. M. Gschwind, R. J. F. Berger and R. Wolf, *J. Am. Chem. Soc.*, 2022, **144**, 20434.
28 A. S. Ionkin, W. J. Marshall, B. M. Fish, A. A. Marchione, L. A. Howe, F. Davidson and C. N. McEwen, *Eur. J. Inorg. Chem.*, 2008, 2386.
29 M. J. Ernst, A. Petrov, M. Weber and C. Müller, *ChemistryEurope*, 2026, **4**, e70252.
30 F. Hennersdorf and J. J. Weigand, *Angew. Chem., Int. Ed.*, 2017, **56**, 7858.
31 (*a*) H. Lei, J. C. Fettinger and P. P. Power, *Organometallics*, 2010, **29**, 5585; (*b*) S. Wang, M. L. McCrea-Hendrick, C. M. Weinstein, C. A. Caputo, E. Hoppe, J. C. Fettinger, M. M. Olmstead and P. P. Power, *J. Am. Chem. Soc.*, 2017, **139**, 6586.
32 (*a*) G. L. Dunn and J. K. Donohue, *Tetrahedron Lett.*, 1968, **9**, 3485; (*b*) G. O. Schenck and R. Steinmetz, *Chem. Ber.*, 1963, **96**, 520.
33 (*a*) M. Hofmann, C. Höhn, F. W. Heinemann and U. Zenneck, *Chem. Eur J.*, 2009, **15**, 5998; (*b*) R. Bartsch, P. B. Hitchcock and J. F. Nixon, *J. Chem. Soc., Chem. Commun.*, 1989, **1046**.
34 C. Schwarzmaier, A. Y. Timoshkin, G. Balázs and M. Scheer, *Angew. Chem., Int. Ed.*, 2014, **53**, 9077.
35 (*a*) W. Huang and P. L. Diaconescu, *Chem. Commun.*, 2012, **48**, 2216; (*b*) S. N. Konchenko, N. A. Pushkarevsky, M. T. Gamer, R. Köppe, H. Schnöckel and P. W. Roesky, *J. Am. Chem. Soc.*, 2009, **131**, 5740; (*c*) M. Scheer, U. Becker and E. Matern, *Chem. Ber.*, 1996, **129**, 721; (*d*) M. E. Barr, B. R. Adams, R. R. Weller and L. F. Dahl, *J. Am. Chem. Soc.*, 1991, **113**, 3052.
36 A. D. Phillips, S. Hino and P. P. Power, *J. Am. Chem. Soc.*, 2003, **125**, 7520.
37 J. R. Pinkes and A. R. Cutler, *Inorg. Chem.*, 1994, **33**, 759.
38 (*a*) CCDC 2529860: Experimental Crystal Structure Determination, 2026, DOI: 10.5517/ccdc.csd.cc2qxjdl; (*b*) CCDC 2529861: Experimental Crystal Structure Determination, 2026, DOI: 10.5517/ccdc.csd.cc2qxjfm; (*c*) CCDC 2529862: Experimental Crystal Structure Determination, 2026, DOI: 10.5517/ccdc.csd.cc2qxjgn; (*d*) CCDC 2529863: Experimental Crystal Structure Determination, 2026, DOI: 10.5517/ccdc.csd.cc2qxjhp; (*e*) CCDC 2529864: Experimental Crystal Structure Determination, 2026, DOI: 10.5517/ccdc.csd.cc2qxjjq; (*f*) CCDC 2529865: Experimental Crystal Structure Determination, 2026, DOI: 10.5517/ccdc.csd.cc2qxjkr; (*g*) CCDC 2529866: Experimental Crystal Structure Determination, 2026, DOI: 10.5517/ccdc.csd.cc2qxjls; (*h*) CCDC 2529867: Experimental Crystal Structure Determination, 2026, DOI: 10.5517/ccdc.csd.cc2qxjmt; (*i*) CCDC 2529868: Experimental Crystal Structure Determination, 2026, DOI: 10.5517/ccdc.csd.cc2qxjnv; (*j*) CCDC 2529869: Experimental Crystal Structure Determination, 2026, DOI: 10.5517/ccdc.csd.cc2qxjpw; (*k*) CCDC 2529870: Experimental Crystal Structure Determination, 2026, DOI: 10.5517/ccdc.csd.cc2qxjqx; (*l*) CCDC 2529871: Experimental Crystal Structure Determination, 2026, DOI: 10.5517/ccdc.csd.cc2qxjry; (*m*) CCDC 2529872: Experimental Crystal Structure Determination, 2026, DOI: 10.5517/ccdc.csd.cc2qxjsz; (*n*) CCDC 2529873: Experimental Crystal Structure Determination, 2026, DOI: 10.5517/ccdc.csd.cc2qxjt0; (*o*) CCDC 2529874: Experimental Crystal Structure Determination, 2026, DOI: 10.5517/ccdc.csd.cc2qxjv1; (*p*) CCDC 2541029: Experimental Crystal Structure Determination, 2026, DOI: 10.5517/ccdc.csd.cc2r94px.